Journal of Cluster Science (2024) 35:1375–1380
https://doi.org/10.1007/s10876-024-02591-3

ORIGINAL PAPER

Perfect Tetrahedral $B_{16}X_4$ (X = P, As) as Non-metal-stabilized Borospherenes with a Truncated B_{16} Cage at the Center

Cai-Yue Gao[1] · Qiao-Qiao Yan[1] · Qiang Chen[1] · Yue-Wen Mu[1] · Si-Dian Li[1]

Received: 27 December 2023 / Accepted: 10 February 2024 / Published online: 16 March 2024

Abstract

Based on extensive global minimum searches augmented with first-principles theory calculations, we predict herein the first boron-based perfect tetrahedral clusters T_d $B_{16}P_4$ (**2**) and T_d $B_{16}As_4$ (**3**) which, as aromatic non-metal analogs of the experimentally observed T_d Au_{20} (2003, *Science* **299**, 864), all contain a truncated T_d B_{16} (**1**) cage at the center effectively stabilized by four trivalent non-metal atoms (P, As) at the corners. Detailed natural bonding orbital (NBO) and adaptive natural density partitioning (AdNDP) bonding analyses indicate that the valences of all the trivalent component atoms in these tetrahedral clusters are fully satisfied, rendering spherical aromaticity and extra stability to the systems. The IR, Raman, and photoelectron spectra (PES) of the concerned species are theoretically simulated to facilitate their characterizations in future experiments.

Graphical Abstract

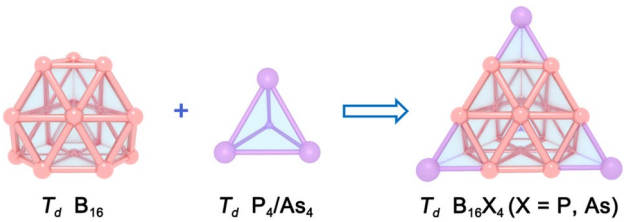

Keywords Borospherenes · First-principles theory · Tetrahedral structures · Bonding patterns · Spectral simulations

Introduction

As the light neighbor of carbon in the periodic table, boron is prototypically electron-deficient and its chemical bonding is dominated by delocalized multicenter-two-electron (mc-2e) bonds in both its polyhedral molecules and bulk allotropes, leading to a great structural diversity in boron-containing systems [1, 2]. Persistent joint photoelectron spectroscopy (PES) and first-principles theory investigations in the past two decades have characterized planar or quasi-planar $B_n^{-/0}$ (n = 3–38 and 40–42) as the dominant isomers in gas phases [3–6], seashell-like $B_{28}^{-/0}$/B_{29}^- and cage-like B_{40}^- as coexisting minor isomers [5, 7, 8], chiral cage-like B_{39}^- as the global minimum of the monoanion [9], and bilayer $B_{48}^{-/0}$ as the global minima for both the neutral and monoanion [10], more specifically, B_{16} as species most concerned in this work possessing elongated quasi-planar C_{2h} structures [3, 4, 11]. The experimentally observed cage-like borospherene B_{40} [5] has been extended to a borospherene family B_n^q (n = 36–42, $q = n$-40) at the first-principles theory level [12–14]. Joint ion-mobility measurements and density functional theory (DFT) investigation indicated that B_n^+ monocations possess double-ring tubular structures in the size range between n = 16-25 [15]. Medium-sized bilayer B_{48}-B_{72} and B_{84}-B_{98},

✉ Qiang Chen
chenqiang@sxu.edu.cn

✉ Yue-Wen Mu
ywmu@sxu.edu.cn

✉ Si-Dian Li
lisidian@sxu.edu.cn

[1] Institute of Molecular Science, Shanxi University, Taiyuan 030006, China

and core-shell B_n ($n = 96$, 111-114, 180, 182, 184) with one or two icosahedral B_{12} cores have been predicted at DFT [16–22]. Recent DFT calculations also indicate that boron is capable of forming highly symmetric clusters in two-dimensional (2D) materials, as in the cases of the theoretically predicted ferromagnetic 2D-B_6 [23] and semiconductor phosphoborane 2D-B_4P_2 [24].

Transition metal-doping has proven to be an effective approach to form various half-sandwich and metallo-borospherenes via effective coordination bonding interactions [25]. The first exohedral metallo-borospherenes $M@B_{40}$ (M =Be, Mg) were predicted in 2015 [26]. Spherical trihedral metallo-borospherenes D_{3h} $La_3B_{18}^-$ with three equivalent deca-coordinate Ta centers as integrated parts of the cage surface was observed in PES experiments in 2020 [27]. Subsequent theoretical research has extended the smallest core-shell metallo-borospherene to D_{3h} $La_3B_{20}^-$ ($La_3[B_2@B_{18}]^-$) [28]. Perfect spherical trihedral D_{3h} $Ta_3B_{12}^-$, tetrahedral T_d Ta_4B_{18}, and tetrahedral T_d La_4B_{24} metallo-borospherenes were also predicted in theory recently [29–31].

However, if non-metal-doping can effectively stabilize high-symmetry B_n cages via covalent bonding interactions still remains unknown to date in both theory and experiments. Inspired by the experimentally observed perfect tetrahedral T_d Au_{20} [32] and based on extensive global searches augmented with first-principles theory calculations, we present herein the possibility of perfect tetrahedral T_d $B_{16}P_4$ (**2**) and T_d $B_{16}As_4$ (**3**) which all possess a truncated tetrahedral T_d B_{16} (**1**) cage at the center effectively stabilized by four trivalent non-metal atoms covalently bounded at the corners. These novel non-metal-stabilized borospherenes as analogs of the observed tetrahedral T_d Au_{20} are expected to be realized in experiments.

Theoretical Methods

Extensive global minimum (GM) searches were performed on $B_{16}P_4$ and $B_{16}As_4$ at PBE/DZVP level using the TGMin2 code [33] and minimum-hopping method [34] implemented in BigDFT package [35, 36]. The six lowest-lying isomers were subsequently optimized at PBE0/6-311+G(d), TPSSh/6-311+G(d) and PBE0/aug-cc-pVTZ level [37–40] using the Gaussian 16 program [41]. Both the hybrid PBE0 and TPSSh methods have proven to be reliable in the characterizations of cage-like boron clusters [5, 7–10]. Frequency checks were performed to ensure that all reported structures are true minima of the systems. Relative energies of the four lowest-lying isomers of neutral were further refined at the coupled cluster CCSD(T)/6-311G(d) level [42–44] implemented in MOLPRO [45] at PBE0/6-311+G(d) geometries. Born-Oppenheimer molecular dynamic (BOMD) simulation at different temperature was implemented employing the CP2K software [46] with the GTH-PBE pseudopotentials and the TZVP-MOLOPTSR-GTH basis set. To eliminate the influence of neighboring molecules on each other, the vacuum space was chosen to be 11 Å. The time of the simulation was set to 30 ps with a time step of 1 fs. Temperature control was performed using the Nose-Hoover method [47]. Natural bonding orbital (NBO) analyses were performed using the NBO 6.0 program [48] and chemical bonding analyses were carried out through the adaptive natural density partitioning (AdNDP) approach [49, 50]. Iso-chemical shielding surfaces (ICSSs) were computed with Multiwfn program [51] and visualized by VMD software [52]. The vertical detachment energies (VDEs) and PES spectra of the monoanions T_d $B_{16}P_4^-$ and T_d $B_{16}As_4^-$ were calculated using the time-dependent DFT (TD-DFT) method [53].

Results and Discussion

Structures and Stabilities

Joint experimental and theoretical investigations have confirmed that T_d P_4 has a perfect tetrahedral geometry as the GM of the neutral, with the valences of all the four trivalent P atoms at the corners fully satisfied [54, 55]. As_4 also proves to have a true T_d GM. Based on the structural motif of the experimentally observed T_d Au_{20} by removing the four corner atoms, we manually constructed in Fig. 1 the perfect truncated tetrahedral T_d B_{16} (**1**) cage composed of four equivalent edge-sharing $B@B_6$ hexagons which, however, as true minimum of the system without imaginary frequencies,

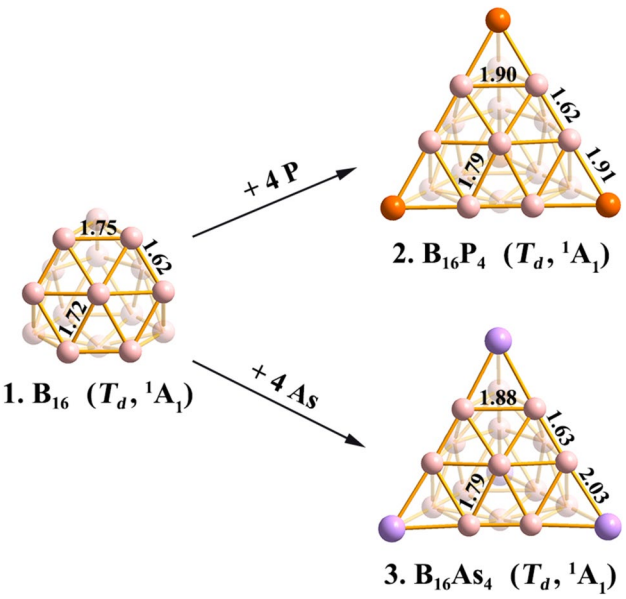

Fig. 1 Optimized structures of T_d B_{16} (**1**), T_d $B_{16}P_4$ (**2**) and T_d $B_{16}As_4$ (**3**) at PBE0/aug-cc-pVTZ level, with the bond lengths indicated in Å

turns out to be much less stable than its elongated quasi-planar C_{2h} B_{16} counterpart observed in experiments [11] due to the existence of unsaturated dangling bonds at the four corners. This situation raises an immediate question on how to effectively stabilize the truncated T_d B_{16} (**1**) by non-metal-doping at the four corners via effective covalent bonding interactions and reminds us to borrow the structural motifs of tetrahedral T_d P_4 and T_d As_4 by covalently capping four trivalent P or As atoms at the four corners of T_d B_{16} (**1**) to fully satisfy the valences of the component atoms. Such a T_d B_{16} + 4 X → T_d $B_{16}X_4$ (X = P, As) strategy proves to work well, as shown in Fig. 1 where both the perfect tetrahedral T_d $B_{16}P_4$ (**2**) and T_d $B_{16}As_4$ (**3**) turned out to be true minima of the systems without imaginary frequencies (Table S1). More encouragingly, extensive global minimum searches utilizing the Tsinghua Global Minimum (TGMin2) package [33] and minima-hopping method [34] implemented in the BigDFT package [35, 36] indicate that, with over 2500 stationary points explored on the potential energy surface, T_d $B_{16}P_4$ (**2**) turned out to be the lowest-lying isomer of the system at PBE0/6-311+G(d), TPSSh/6-311+G(d), and PBE0/aug-cc-pVTZ levels [37–40] implemented in Gassian16 program [41] and CCSD(T)/6-311G(d) [42–44] implemented in MOLPRO package [45] (Fig. S1). As demonstrated in Fig. S1, with zero-point corrections considered, the most concerned T_d $B_{16}P_4$ (**2**) and its planar isomer C_{2h} $B_{16}P_4$ lie within 0.01 eV at 0 K at the most accurate CCSD(T)/6-311G(d) level performed in this work, they are therefore practically iso-energetic isomers possible to coexist in experiments, while the third C_1 $B_{16}P_4$ (^{1}A), fourth C_1 $B_{16}P_4$ (^{1}A) and fifth C_2 $B_{16}P_4$ (^{1}A) cage-like isomers turn out to be 0.47, 0.50, 0.60 eV less stable than T_d $B_{16}P_4$ (**2**) in relative energies at CCSD(T), respectively. A similar relative energy order exists in neutral $B_{16}As_4$, where the planar C_{2h} $B_{16}As_4$ appears to be 0.64 eV more stable than T_d $B_{16}As_4$ (**3**) at 0 K (Fig. S2) at CCSD(T). However, previous gas-phase PES experiments have shown that temperature (entropy) effects play an important role in determining the relative populations of the low-lying isomers [56]. In the cases concerned in this work, as shown in Fig. S3, T_d $B_{16}P_4$ (**2**) appears to be 0.40, 0.36, 0.28, 0.19, 0.10 and 0.01 eV more stable than its planar C_{2h} counterpart at 0 K, 100 K, 200 K, 298 K, 400 K, and 500 K at PBE0 level in terms of Gibbs free energies with entropy effects considered, respectively, strongly suggesting that T_d $B_{16}P_4$ (**2**) may serve as the dominant isomer with the highest population in gas-phase experiments below 500 K. Similarly, as shown in Fig. S3, T_d $B_{16}As_4$ (**3**) turns out to be 0.13, 0.08, and 0.01 eV more stable than its planar C_{2h} $B_{16}As_4$ counterpart at 0 K,100 K, and 200 K in Gibbs free energies, respectively, indicating that T_d $B_{16}As_4$ (**3**) may be the most highly populated isomer in gas-phase experiments below 200 K as well. We also notice that the high-symmetry T_d $B_{16}P_4$ (**2**) and T_d $B_{16}As_4$ (**3**) as non-metal-stabilized borospherenes possess the large calculated HOMO-LUMO energy gaps of ΔE_{gap} = 3.31 and 3.16 eV at PBE0/aug-cc-pVTZ level, respectively (Table S1) which are even obviously bigger than that (1.77 eV) of the experimentally observed tetrahedral T_d Au_{20} [32], suggesting that these unusual species are highly chemically inert and possible to be synthesized and characterized in experiments. Detailed natural bonding orbital (NBO) analyses [48] show that the four equivalent hexa-coordinate central boron atoms (HCB) on four triangular faces, twelve equivalent hexa-coordinate edging B atoms (HEB) on six edges, and four trivalent corner P atoms (TCP) at four corners of T_d $B_{16}P_4$ (**2**) possess the calculated total Wiberg bond indexes of WBI_{HCB} = 3.45, WBI_{HEB} = 3.82 and WBI_{TCP} = 3.10, respectively (Table S1), indicating that the valences of all the trivalent component atoms are fully satisfied. Similar situation exists in T_d $B_{16}As_4$ (**3**).

Extensive molecular dynamic (MD) simulations using the CP2K package [46] indicate that these tetrahedral species are highly dynamically stable at high temperatures as well, as demonstrated in the cases of T_d $B_{16}P_4$ (**2**) and T_d $B_{16}As_4$ (**3**) which have the small calculated average root-mean-square-deviations of RMSD = 0.15, 0.14 Å and maximum bond length deviations of MAXD = 0.48, 0.45 Å at 1200 K and 1000 K, respectively (Fig. S4). No other low-lying isomers are observed during the MD simulations in 30 ps.

Chemical Bonding and Spherical Aromaticity Analyses

To better interpret the high stabilities of these tetrahedral species, we performed detailed adaptive natural density partitioning (AdNDP) bonding analyses [49, 50] on T_d $B_{16}P_4$ (**2**) and T_d $B_{16}As_4$ (**3**) to unveil their bonding patterns. As shown in Fig. 2a, $B_{16}P_4$ (**2**) possesses 4 equivalent 1c-2e lone pairs (LPs) with the occupation number of ON = 1.90 |e| on the four corner P atoms, 12 equivalent localized 2c-2e B-P σ bonds with ON = 1.85 |e| between the trivalent P atoms and corner B atoms of the truncated B_{16} cage, and 12 equivalent delocalized 3c-2e σ bonds with ON = 1.81 |e| over twelve B_3 triangles on the truncated T_d B_{16} cage. The remaining 6 equivalent 4c-2e σ bonds with ON = 1.91 |e| are delocalized over six B_4 tetrahedrons evenly distributed inside the truncated T_d B_{16} cage along the six edges. The bonding pattern difference between our T_d $B_{16}P_4$ (**2**) with six 4c-2e σ bonds and the previously reported T_d Au_{20} with ten 4c-2e σ bonds mainly occurs at the four corners, with the former having three 2c-2e B-P σ bonds at each corner to fully satisfy simultaneously the valences of the trivalent P atom and its three neighboring B atoms in the truncated B_{16} cage, while the latter possessing one 4c-2e σ bond delocalized over each Au_4 tetrahedron at the corner [57]. Such a bonding pattern well reflects the importance to covalently incorporate four

trivalent P atoms at the four corners of the T_d B_{16} cage. As demonstrated in Fig. 1 and Fig. S1–S2, the four covalently bonded trivalent atoms of P and As at the four corners best serve the purpose to stabilize a truncated T_d B_{16} (**1**) cage at the center. As expected, T_d $B_{16}As_4$ (**3**) possesses a similar bonding pattern with T_d $B_{16}P_4$ (**2**) (Fig. 2b), indicating that the trivalent P and As possess essentially the same bonding capacities.

Such unique bonding patterns render spherical aromaticity and extra stability to the systems, as evidenced by the calculated negative nucleus-independent chemical shift (NICS) [58, 59] values of NICS = − 41 ppm and − 37 ppm at the cage centers of $B_{16}P_4$ (**2**) and $B_{16}As_4$ (**3**), respectively (Table S1). The spherical aromatical nature of $B_{16}P_4$ (**2**) and $B_{16}As_4$ (**3**) is further demonstrated by their iso-chemical shielding surfaces (ICSSs) based on the calculated NICS-ZZ components depicted in Fig. 3, where the yellow areas with negative NICS-ZZ values inside the T_d tetrahedron and within about 1.0 Å above the cage surface in the vertical direction belong to chemical shielding regions, while the green regions with positive NICS-ZZ values like a belt around the waist in horizontal directions belong to chemical de-shielding regions. The ICSSs of both T_d $B_{16}P_4$ (**2**) and T_d $B_{16}As_4$ (**3**) (Fig. 3 a, b) appear to be similar to that of the experimentally observed spherically aromatical D_{2d} B_{40} [5] (Fig. 3c), well indicating the spherical aromatic nature of the perfect tetrahedral T_d $B_{16}X_4$ species (X = P, As).

Spectral Simulations

The IR and Raman spectra of $B_{16}P_4$ (**2**) and $B_{16}As_4$ (**3**) and PES spectra of the corresponding optimized perfect tetrahedral T_d $B_{16}P_4^-$ and T_d $B_{16}As_4^-$ are theoretically simulated at PBE0/aug-cc-pVTZ in Fig. 4 to facilitate their future experimental characterizations. The high-symmetry T_d $B_{16}P_4$ (**2**) exhibits highly simplified IR and Raman spectra (Fig. 4a), with two major IR active peaks at 572 (t_2) and 1190 (t_2) cm^{-1} and four strong Raman peaks at 404 (t_2), 421 (a_1), 485 (a_1), and 619 (a_1) cm^{-1}, respectively, with the Raman peak at 619 (a_1) cm^{-1} representing the typical "radial breathing mode" (RBM) of the cage-like structure which can be used to characterize hollow cage geometries [60]. In the simulated PES spectrum of T_d $B_{16}P_4^-$ in Fig. 4b, the first vertical detachment energy at VDE_1 = 2.68 eV represents the energy difference between the neutral and monoanion at the optimized anionic geometry. The large gap of 1.59 eV between VDE_1 and VDE_2 (4.27 eV) reflects the existence of the huge HOMO-LUMO gap in T_d $B_{16}P_4$ (**2**) as discussed above. Other higher VDEs at 4.71, 4.78, 5.07, and 5.17 eV correspond to vertical electronic transitions from the ground state of the monoanion to the excited states of the neutral at the anion geometry. $B_{16}As_4$ (**3**) (Fig. 4c) and $B_{16}As_4^-$ (Fig. 4d)

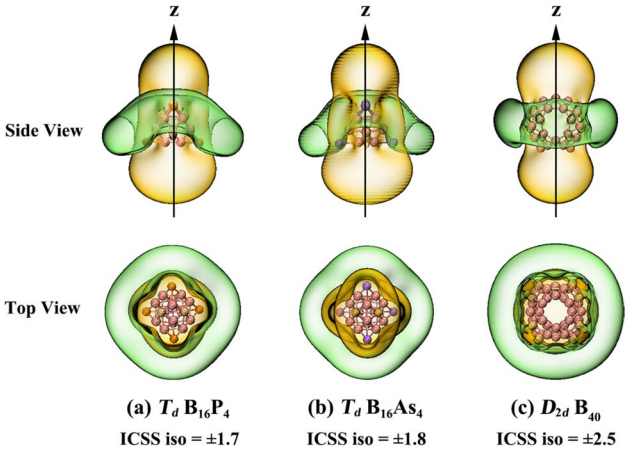

Fig. 3 Iso-chemical shielding surfaces (ICSSs) of **a** T_d $B_{16}P_4$ (**2**) and **b** T_d $B_{16}As_4$ (**3**), compared with that of the observed spherically aromatic **c** D_{2d} B_{40}

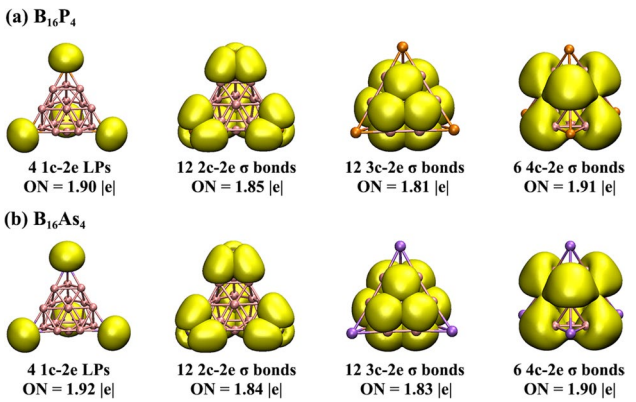

Fig. 2 AdNDP bonding patterns of **a** T_d $B_{16}P_4$ (**2**) and **b** T_d $B_{16}As_4$ (**3**) with the occupation numbers (ON) indicated

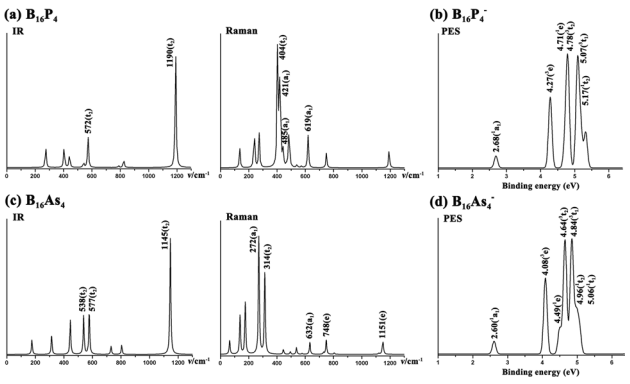

Fig. 4 Simulated IR and Raman spectra of **a** T_d $B_{16}P_4$ (**2**) and **c** T_d $B_{16}As_4$ (**3**) and PES spectra of **b** T_d $B_{16}P_4^-$ and **d** T_d $B_{16}As_4^-$ at PBE0/aug-cc-pVTZ

exhibit similar spectral features with T_d $B_{16}P_4$ (**2**) and T_d $B_{16}P_4^-$, respectively.

Conclusions

In summary, we have predicted at first-principles theory level in this work the perfect tetrahedral non-metal-stabilized borospherenes T_d $B_{16}P_4$ (**2**) and T_d $B_{16}As_4$ (**3**) as non-metal analogs of the experimentally characterized tetrahedral T_d Au_{20}. These tetrahedral structures fully satisfy the valences of all the trivalent component atoms, making them spherically aromatic in nature. Gas-phase experimental syntheses and characterizations of the theoretically predicted high-symmetry T_d $B_{16}X_4$ species by laser-ablations of mixed B-X targets (X = P, As) will help to enrich the structures and bonding of boron. Such tetrahedral species or their derivatives may serve as building blocks in bottom-up approaches to form novel low-dimensional non-metal-dopped boride nanomaterials.

Supplementary Information The online version contains supplementary material available at https://doi.org/10.1007/s10876-024-02591-3.

Author Contributions Si-Dian Li, Qiang-Chen and Yue-Wen Mu designed the project and finalized the manuscript; Cai-Yue Gao and Qiao-Qiao Yan performed the calculations and prepared the first draft. All authors read and approved the final manuscript.

Funding This work was supported by the National Natural Science Foundation of China (22373061 and 21973057 to S.-D. L; 22003034 to Q. C).

Data Availability The data presented in this article are available on request from the corresponding author.

Declarations

Competing interest The authors declare no conflict of interest.

Ethical Approval Not applicable.

References

1. A. R. Oganov, J. H. Chen, C. Gatti, Y. Z. Ma, Y. M. Ma, C. W. Glass, Z. X. Liu, T. Yu, O. O. Kurakevych, and V. L. Solozhenko (2009). *Nature* **460**, 292.
2. A. P. Sergeeva, I. A. Popov, Z. A. Piazza, W. L. Li, C. Romanescu, L. S. Wang, and A. I. Boldyrev (2014). *Acc. Chem. Res.* **47**, 1349.
3. T. Jian, X. N. Chen, S. D. Li, A. I. Boldyrev, J. Li, and L. S. Wang (2019). *Chem. Soc. Rev.* **48**, 3550.
4. L. S. Wang (2016). *Int. Rev. Phys. Chem.* **35**, 69.
5. H. J. Zhai, Y. F. Zhao, W. L. Li, Q. Chen, H. Bai, H. S. Hu, Z. A. Piazza, W. J. Tian, H. G. Lu, Y. B. Wu, Y. W. Mu, G. F. Wei, Z. P. Liu, J. Li, S. D. Li, and L. S. Wang (2014). *Nat. Chem.* **6**, 727.
6. H. Bai, T. T. Chen, Q. Chen, X. Y. Zhao, Y. Y. Zhang, W. J. Chen, W. L. Li, L. F. Cheung, B. Bai, J. Cavanagh, W. Huang, S. D. Li, J. Li, and L. S. Wang (2019). *Nanoscale* **11**, 23286.
7. Y. J. Wang, Y. F. Zhao, W. L. Li, T. Jian, Q. Chen, X. R. You, T. Ou, X. Y. Zhao, H. J. Zhai, S. D. Li, J. Li, and L. S. Wang (2016). *J. Chem. Phys.* **144**.
8. L. Pei, H. R. Li, M. Yan, Q. Chen, Y. W. Mu, H. G. Lu, Y. B. Wu, and S. D. Li (2018). *Phys. Chem. Chem. Phys.* **20**, 15330.
9. Q. Chen, W. L. Li, Y. F. Zhao, S. Y. Zhang, H. S. Hu, H. Bai, H. R. Li, W. J. Tian, H. G. Lu, H. J. Zhai, S. D. Li, J. Li, and L. S. Wang (2015). *Acs Nano* **9**, 754.
10. W. J. Chen, Y. Y. Ma, T. T. Chen, M. Z. Ao, D. F. Yuan, Q. Chen, X. X. Tian, Y. W. Mu, S. D. Li, and L. S. Wang (2021). *Nanoscale* **13**, 3868.
11. A. P. Sergeeva, D. Y. Zubarev, H. J. Zhai, A. I. Boldyrev, and L. S. Wang (2008). *J. Am. Chem. Soc.* **130**, 7244.
12. W. J. Tian, Q. Chen, H. R. Li, M. Yan, Y. W. Mu, H. G. Lu, H. J. Zhai, and S. D. Li (2016). *Phys. Chem. Chem. Phys.* **18**, 9922.
13. H. Liu, Y.-W. Mu, and S.-D. Li (2022). *J. Clust. Sci.* **33**, 81.
14. Q. Chen, S. Y. Zhang, H. Bai, W. J. Tian, T. Gao, H. R. Li, C. Q. Miao, Y. W. Mu, H. G. Lu, H. J. Zhai, and S. D. Li (2015). *Angew. Chem. Int. Ed.* **54**, 8160.
15. E. Oger, N. R. M. Crawford, R. Kelting, P. Weis, M. M. Kappes, and R. Ahlrichs (2007). *Angew. Chem. Int. Ed.* **46**, 8503.
16. L. Pei, Q. Q. Yan, and S. D. Li (2021). *Eur. J. Inorg. Chem.* **26**, 2618.
17. Q. Q. Yan, L. Pei, and S. D. Li (2021). *J. Mol. Model.* **27**, 364.
18. Q. Q. Yan, T. Zhang, Y. Y. Ma, Q. Chen, Y. W. Mu, and S. D. Li (2022). *Nanoscale* **14**, 11443.
19. Y. Y. Ma, X. Y. Zhao, W. Y. Zan, Y. W. Mu, Z. H. Zhang, and S. D. Li (2022). *Nano Res.* **15**, 5752.
20. L. W. Sai, X. Wu, and F. Y. Li (2022). *Phys. Chem. Chem. Phys.* **24**, 15687.
21. M. Zhang, H. G. Lu, and S. D. Li (2021). *Nano Res.* **14**, 4719.
22. M. Zhang, W.-P. Jia, T. Zhang, B.-B. Pei, J. Xu, X. Tian, H.-G. Lu, and S. D. Li (2022). *Sci. Rep.* **12**, 19741.
23. D. V. Steglenko, N. V. Tkachenko, A. I. Boldyrev, R. M. Minyaev, and V. I. Minkin (2020). *J. Comput. Chem.* **41**, 1456.
24. N. V. Tkachenko, D. Steglenko, N. Fedik, N. M. Boldyreva, R. M. Minyaev, V. I. Minkin, and A. I. Boldyrev (2019). *Phys. Chem. Chem. Phys.* **21**, 19764.
25. J. Barroso, S. Pan, and G. Merino (2022). *Chem. Soc. Rev.* **51**, 1098.
26. H. Bai, Q. Chen, H. J. Zhai, and S. D. Li (2015). *Angew. Chem. Int. Ed.* **54**, 941.
27. T. T. Chen, W. L. Li, W. J. Chen, X. H. Yu, X. R. Dong, J. Li, and L. S. Wang (2020). *Nat. Commun.* **11**, 2766.
28. X. Y. Zhao, M. Yan, Z. H. Wei, and S. D. Li (2020). *Rsc Adv.* **10**, 34225.
29. Y. Zhang, X. Y. Zhao, M. Yan, and S. D. Li (2020). *Rsc Adv.* **10**, 29320.
30. Y. Zhang, X. Q. Lu, M. Yan, and S. D. Li (2021). *Acs Omega* **6**, 10991.
31. X. Q. Lu, C. Y. Gao, Z. H. Wei, and S. D. Li (2021). *J. Mol. Model.* **27**, 130.
32. J. Li, X. Li, H. J. Zhai, and L. S. Wang (2003). *Science* **299**, 864.
33. Y. F. Zhao, X. Chen, and J. Li (2017). *Nano Res.* **10**, 3407.
34. S. Goedecker (2004). *J. Chem. Phys.* **120**, 9911.
35. L. Genovese, A. Neelov, S. Goedecker, T. Deutsch, S. A. Ghasemi, A. Willand, D. Caliste, O. Zilberberg, M. Rayson, A. Bergman, and R. Schneider (2008). *J. Chem. Phys.* **129**.
36. A. Willand, Y. O. Kvashnin, L. Genovese, A. Vázquez-Mayagoitia, A. K. Deb, A. Sadeghi, T. Deutsch, and S. Goedecker (2013). *J. Chem. Phys.* **138**.
37. C. Adamo and V. Barone (1999). *J. Chem. Phys.* **110**, 6158.
38. V. N. Staroverov, G. E. Scuseria, J. M. Tao, and J. P. Perdew (2003). *J. Chem. Phys.* **119**, 12129.
39. R. Krishnan, J. S. Binkley, R. Seeger, and J. A. Pople (1980). The. *J. Chem. Phys.* **72**, 650.

40. R. A. Kendall, T. H. Dunning, and R. J. Harrison (1992). *J. Chem. Phys.* **96**, 6796.
41. M. J. Frisch, et al., *Gaussian 16, Revision A.03* (Gaussian Inc., Wallingford CT, 2016).
42. G. D. Purvis and R. J. Bartlett (1982). *J. Chem. Phys.* **76**, 1910.
43. J. Čížek (1969). *Adv. Chem. Phys.* **14**, 35.
44. K. Raghavachari, G. W. Trucks, J. A. Pople, and M. Head-Gordon (1989). *Chem. Phys. Lett.* **157**, 479.
45. H. J. Werner, P. J. Knowles, G. Knizia, F. R. Manby, and M. Schutz (2012). *Wiley Interdiscip. Rev: Comput. Mol. Sci.* **2**, 242.
46. J. V. Vondele, M. Krack, F. Mohamed, M. Parrinello, T. Chassaing, and J. Hutter (2005). *Comput. Phys. Commun.* **167**, 103.
47. G. J. Martyna, M. L. Klein, and M. Tuckerman (1992). *J. Chem. Phys.* **97**, 2635.
48. P. E. D. Glendening, J. K. Badenhoop, A. E. Reed, J. E. Carpenter, J. A. Bohmann, C. M. Morales, C. R. Landis, and F. Weinhold (2013). *J. Coordin. Chem.* **72**, 2215.
49. D. Y. Zubarev and A. I. Boldyrev (2008). *Phys. Chem. Chem. Phys.* **10**, 5207.
50. N. V. Tkachenko and A. I. Boldyrev (2019). *Phys. Chem. Chem. Phys.* **21**, 9590.
51. T. Lu and F. Chen (2012). *J. Comput. Chem.* **33**, 580.
52. W. Humphrey, A. Dalke, and K. Schulten (1996). *J. Mol. Graph.* **14**, 33.
53. R. Bauernschmitt and R. Ahlrichs (1996). *Chem. Phys. Lett.* **256**, 454.
54. R. O. Jones, G. Gantefor, S. Hunsicker, and P. Pieperhoff (1995). *J. Chem. Phys.* **103**, 9549.
55. R. O. Jones and D. Hohl (1990). *J. Chem. Phys.* **92**, 6710.
56. H. R. Li, T. Jian, W. L. Li, C. Q. Miao, Y. J. Wang, Q. Chen, X. M. Luo, K. Wang, H. J. Zhai, S. D. Li, and L. S. Wang (2016). *Phys. Chem. Chem. Phys.* **18**, 29147.
57. D. Y. Zubarev and A. I. Boldyrev (2009). *J. Phys. Chem. A* **113**, 866.
58. P. V. Schleyer, C. Maerker, A. Dransfeld, H. J. Jiao, and N. Hommes (1996). *J. Am. Chem. Soc.* **118**, 6317.
59. Z. F. Chen, C. S. Wannere, C. Corminboeuf, R. Puchta, and P. V. Schleyer (2005). *Chem. Rev.* **105**, 3842.
60. D. Ciuparu, R. F. Klie, Y. M. Zhu, and L. Pfefferle (2004). *J. Phys. Chem. B* **108**, 3967.